Palaeogeography, Palaeoclimatology, Palaeoecology 635 (2024) 111945

Contents lists available at ScienceDirect

Palaeogeography, Palaeoclimatology, Palaeoecology

journal homepage: www.elsevier.com/locate/palaeo

Decreased Westerly moisture transport leads to abrupt vegetation change in northern Central Asia during late MIS3: Evidence from Zeketai Loess, Ili Basin

Shijin Zhao [a,b], Francien Peterse [b], Chongyi E [c], Yanyan Lei [a], Miao Huang [a], Huan Yang [d,*], Shucheng Xie [a]

[a] State Key Laboratory of Biogeology and Environmental Geology, School of Earth Sciences, China University of Geosciences, Wuhan 430074, China
[b] Department of Earth Sciences, Utrecht University, 3584 CB Utrecht, the Netherlands
[c] Qinghai Provincial Key Laboratory of Physical Geography and Environmental Processes, School of Geographic Science, Qinghai Normal University, Xining 810008, China
[d] Hubei Key Laboratory of Critical Zone Evolution, School of Geography and Information Engineering, China University of Geosciences, Wuhan 430074, China

ARTICLE INFO

Editor: Dr. Paul Hesse

Keywords:
Northern Central Asia
Hydroclimate
Ili loess
Marine isotope stage 3
Stable carbon isotope
Westerlies

ABSTRACT

Moisture transportation to (semi-)arid Central Asia is influenced by the interplay of multiple atmospheric circulation patterns. The mechanism underlying the hydroclimate evolution in CA has recently received increasing attention. In northeastern CA, most of the precipitation falls in summer, counter to other westerly-dominated regions of CA where precipitation maximizes in boreal winter. The marine isotope stage (MIS) 3 offers a unique opportunity to examine the mechanisms driving hydroclimate variations during warm periods of the ice age in the CA. However, due in part to reliable proxies for reconstruction, the hydroclimate and vegetation change during MIS3 in northeastern CA have not been well studied. Here, we use grain size and magnetic susceptibility data from the Zeketai loess profile to reconstruct historical shifts in precipitation patterns during MIS3 in the Ili Basin from arid Central Asia (ACA). Notably, abrupt changes around 35 ka are evident in the grain size and magnetic susceptibility records, reflecting a transition to reduced wind intensity and increased aridity. Subsequent analysis of plant leaf waxes (*n*-alkanes), hydrogen isotopic composition of *n*-alkanes ($\delta D_{n\text{-alkane}}$), and stable carbon isotope ratios of total organic carbon ($\delta^{13}C_{org}$) within the loess profile indicates a concurrent shift towards more shrubs, aligning with reduced moisture availability. The $\delta^{13}C_{org}$ record further elucidates that during MIS3, the Ili Basin predominantly harbored C_3 vegetation. However, the alteration in $\delta^{13}C_{org}$ and $\delta D_{n\text{-alkane}}$ to more positive values at approximately 35 ka substantiates the transition to more drought-resistant vegetation. Furthermore, we link the paleo-hydroclimate variations to the decrease in solar radiation and the strengthening of the Atlantic Meridional Overturning Circulation (AMOC) and Siberian High during late MIS3. This joint influence weakens the Westerly winds and subsequently diminishes the conveyance of moisture to CA.

1. Introduction

Central Asia (CA) spans a vast area from the Caspian Sea in the west to northwest China in the east, characterized predominantly by a (semi-) arid continental climate. Given the limitation in water resources, gaining an improved understanding of the hydroclimate evolution and its driving factors holds significant importance for fostering sustainable agriculture practices and the protection of vulnerable ecosystems across CA. The modern (hydro)climate in arid Central Asia (ACA) is dominated by the Westerlies, a wind system that forms a connection between the polar air masses within the Northern Hemisphere and East Asia. In southwestern ACA, the westerlies are associated with (semi)arid conditions, and most of the precipitation falls during winter and spring in the northwest (Xu et al., 2010), while in the northeast, precipitation maximizes during summer (Zhao et al., 2022). This contrasts starkly with East Asia, where the influence of the East Asian Summer Monsoon (EASM) prevails, ushering in warmer and more humid climatic conditions with the majority of precipitation falling during summer (e.g., Chen et al., 2015; Wang et al., 2017).

While the Pleistocene precipitation dynamics of monsoonal East Asia

* Corresponding author.
E-mail address: yhsailing@163.com (H. Yang).

https://doi.org/10.1016/j.palaeo.2023.111945
Received 14 January 2023; Received in revised form 3 November 2023; Accepted 27 November 2023
Available online 30 November 2023

have been extensively documented through cave speleothems (e.g., Cheng et al., 2009; Wang et al., 2001) and loess-paleosol sequences from the Chinese Loess Plateau (CLP) (e.g., Guo et al., 2002), the hydroclimate study of Westerlies-dominated areas has primarily focused on the Holocene (Chen et al., 2008, 2019) and the Last Glacial Maximum (Li et al., 2022). The hydrological history of other Quaternary periods in CA has received comparatively less attention, due in part to reliable proxies for precipitation reconstruction, hindering a comprehensive understanding of hydroclimate dynamics within CA.

The marine isotope stage (MIS) 3 (57–24 ka B.P.), represents an interstadial during the last glaciation, marked by a series of abrupt millennial-scale climatic transitions observed in the North Atlantic, e.g. colder Heinrich (H) events and warmer Dansgaard–Oeschger (D—O) events (North Greenland Ice Core Project members, 2004). Commonly referred to as the Bond cycle, these climatic transitions typically commenced with two successive warmer D—O events and culminated in a colder Heinrich event, each persisting for approximately 10 to 15 ka (Agosta and Compagnucci, 2016). Despite MIS3 being a relatively warmer stage during the glacial period, the global ice volume and northern hemispheric solar insolation during this period significantly differ from those of the Holocene. As a result, MIS3 offers a distinctive opportunity to examine the underlying mechanisms driving hydroclimate variations during relatively warm periods of the ice age in the CA.

Loess deposits that are widely distributed in CA may provide climate archives to document the paleoclimate changes during the MIS3. Examination of loess proxy records from northern CA throughout the last glaciation has revealed the presence of several millennial-scale abrupt climatic events that can be linked to the Greenland ice core record (Ye et al., 2000; Li et al., 2016; Song et al., 2018), suggesting that they are suitable archives of sub-orbital scale climate variations. In the Ili Basin, the clay component (< 4 μm) (Fig. 1A, E et al., 2014) or fine fraction (< 10 μm) (TLD, Fig. 1A, Zhang et al., 2015) of the loess profile experienced a decrease, mirroring analogous changes observed in oxygen isotope records from Greenland ice cores during Younger Dryas and Heinrich events. Similar findings were observed in the Zhaosu loess Section (ZSP, Fig. 1A) in the upper reaches of the Tekes River region, suggesting a potential connection between CA and North Atlantic climate patterns on the millennial scale (Song et al., 2018). Meanwhile, investigations into the Nilek Loess profile (NLK, Fig. 1A) along the Kashi River bench

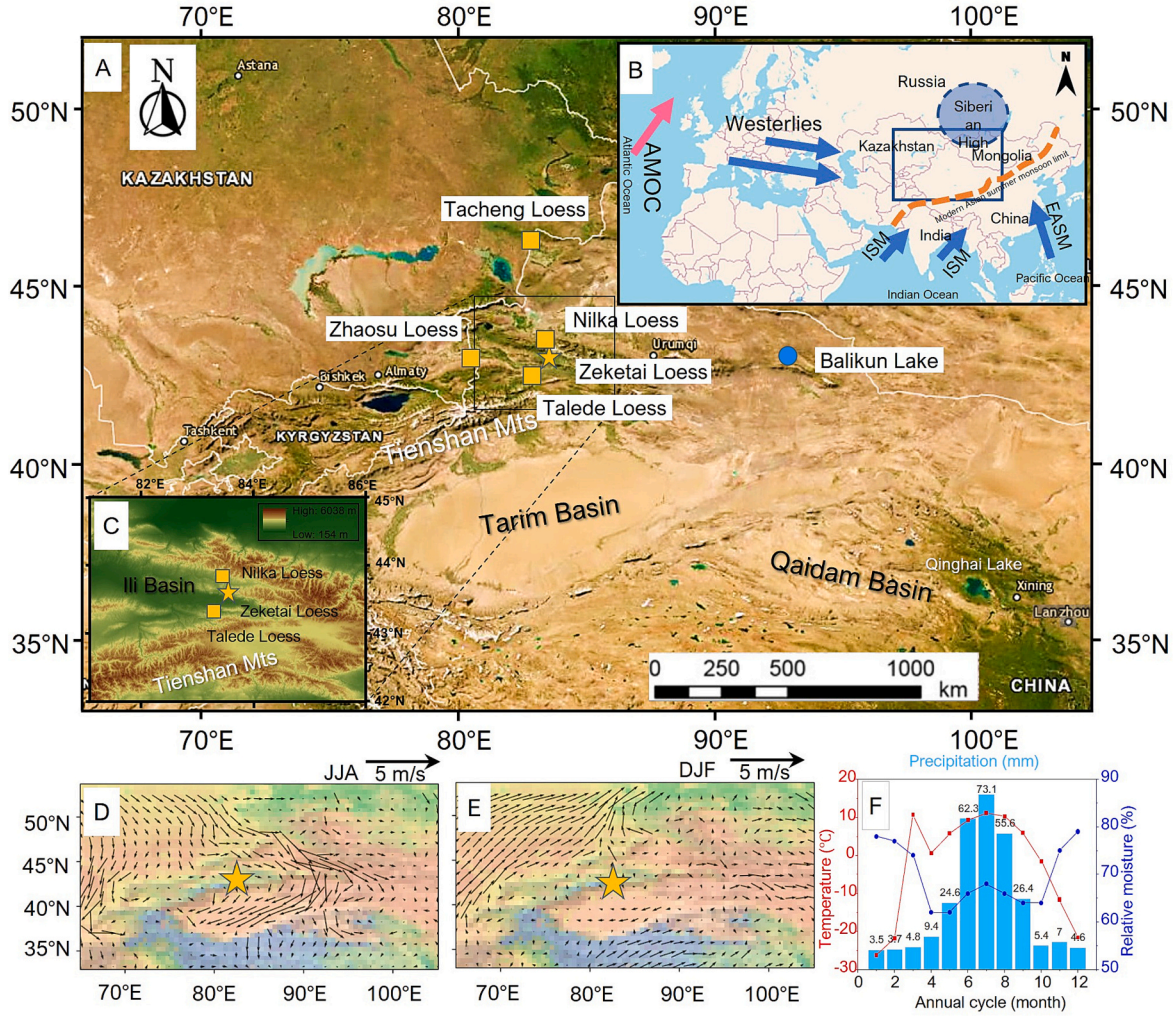

Fig. 1. (A) Geographical context of the Zeketai loess section (yellow star) in northwest China. Locations of other MIS3 records used for comparison are also shown: Tacheng loess (Li et al., 2019), Zhaosu loess (Song et al., 2018), Talede loess (Zhang et al., 2015), Nilka loess (Li et al., 2018), Balikun lake (Zhao et al., 2017); (B) Location of the study area (rectangle), and the climatic circulation systems including Atlantic Meridional Overturning Circulation (AMOC), the Westerlies, Siberian High, and East Asia summer monsoon (EASM) are also shown; (C) DEM map showing local geomorphic context of the study area; (D) & (E) Mean 850 hPa (~1500 m a.s.l.) streamline (5 m/s) in study region for the year 1979–2019 (data from the European Centre for Medium-Range Weather Forecasts (ECMWF) *Re*-Analysis (ERA)-Interim data sets, Hersbach et al. (2019), (D) and (E) show the circulation in summer (JJA) and winter (DJF), respectively. The yellow pentagram indicates the location of the Zeketai (ZKT) loess; (F) averaged monthly precipitation, moisture, and temperature in the nearest meteorological station Bayanbulak for the year 1980–2010 (data from http://data.cma.cn). (For interpretation of the references to color in this figure legend, the reader is referred to the web version of this article.)

indicated that, in addition to mid-latitude westerly winds, abrupt climate signals can also be conveyed from the high latitudes of the Northern Hemisphere through the Siberian high (Li et al., 2018). Despite these efforts to explore the paleoclimate over the last glaciation, the paleoclimate evolution, in particular, the hydroclimate, during MIS3 is still poorly characterized.

Here we aim to reconstruct the climate history of northern CA during MIS3, a period characterized by millennial-scale changes in the North Atlantic (Wang et al., 2008), based on the Zeketai loess section in the Ili Basin of northwest China (Fig. 1). The 22.5-m-thick Zeketai loess section covers the past 77,000 years (E et al., 2014). However, the uppermost layer exhibits disturbances and the optically stimulated luminescence (OSL) signal in layers below 11 m has reached saturation. Consequently, our focus rests on the interval between 2 and 11 m, corresponding to a timeframe of 19 to 54 ka. This study combined the existing grain size data for this section (E et al., 2014) with magnetic susceptibility to generate continuous, high-resolution records of the Westerlies (as reflected by grain size) and precipitation intensity (reflected by magnetic susceptibility) in CA during MIS3. Furthermore, an assessment of vegetation response to reconstructed (hydro)climatic changes in CA is conducted by analyzing the stable carbon isotopic composition of the total organic carbon (TOC), as well as the assemblage of plant leaf waxes (*n*-alkanes) and their stable hydrogen isotope ($\delta D_{n\text{-alkane}}$) stored in the same loess section.

2. Material and methods

2.1. Site description and sample collection

The Zeketai section (43°32′14′N, 83°18′50″E; ~1000 m a.s.l.) is located at the alluvial and diluvial terraces on the north bank of the Kunse River, a tributary of Ili River, north of the Tianshan foothills. The site is next to the Zeketai Brick Factory, merely 1 km east of Zeketai Town in Xinyuan County of the Xinjiang Uygur Autonomous Region, China (Fig. 1 for geographical context). The mean annual temperature in Xinyuan region is 8 °C and mean annual precipitation is 480 mm, with an approximate annual potential evaporation of 1200 mm;E et al., 2014). The airmass prevailing at altitudes ≥1.5 km a.s.l. (850 hPa) is consistently influenced by the westerly jet stream (Fig. 1D, E), whereas closer to the ground, the prevailing wind direction is predominately from the east (E et al., 2014). The Zeketai section is covered by typical steppe vegetation, dominated by Gramineae and Artemisia.

The upper 11 m of the Zeketai section consists of a sequence of Holocene soil (indicated by black bar in Fig. 2), alternating loess (light gray bar in Fig. 2), and paleosol layers (dark gray bar in Fig. 2). The upper Holocene soil layer (0–1 m, dated at 13.28 ± 1.00 ka at 1 m, all OSL ages from E et al., 2014) is enriched in organic matter and carbonate, overlaying a light-yellow loess layer (1–6 m, 13.28 ± 1.00 ka to 34.78 ± 2.92 ka; corresponding to MIS2 and MIS3a), which is relatively dense and has no visible traces of biological activity. Under that lies a weakly developed paleosol layer (6–9 m, 34.78 ± 2.92 ka to interpolated 47.76 ka; denoted as MIS3b), possessing a similar color to the preceding layer yet displaying higher organic matter and similar carbonate concentrations. Subsequently, a consolidated yellowish loess layer (9–11 m, interpolated 47.76 ka to 54.51 ± 4.22 ka; designated as MIS3c) is encountered. This stratum exhibits limited organic matter and carbonate content while presenting no discernible indications of biological activity.

For this study, a total of 227 samples were collected at 5 cm resolution within the interval between 2 and 11.2 m in 2010, yielding an average resolution of ~200 years. The uppermost 2 m of the section has been disturbed by anthropogenic activity and is therefore not included in this study. The age-depth model was determined by linear interpolation using the OSL ages from E et al. (2014) (Fig. 2). The grain size (Fig. 3A) and TOC (Fig. 3B) of these samples have been documented in a previous study by E et al. (2014).

2.2. Magnetic susceptibility

All samples were dried in an oven at 45 °C, then gently ground to

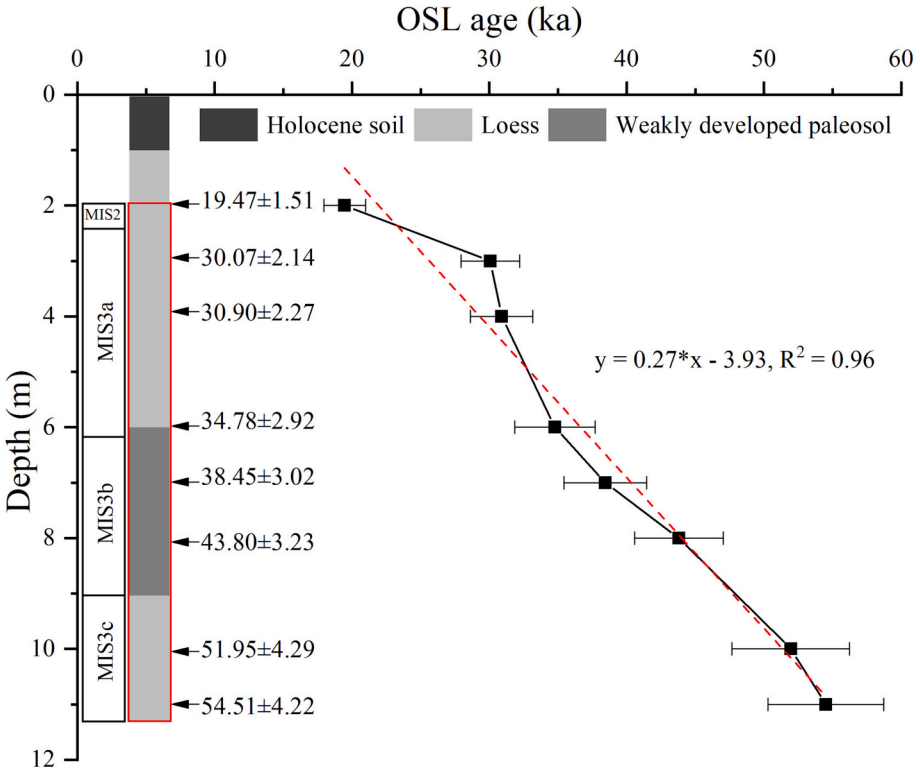

Fig. 2. Linear interpolation age-depth model of the Zeketai section based on previous OSL ages (E et al., 2014).

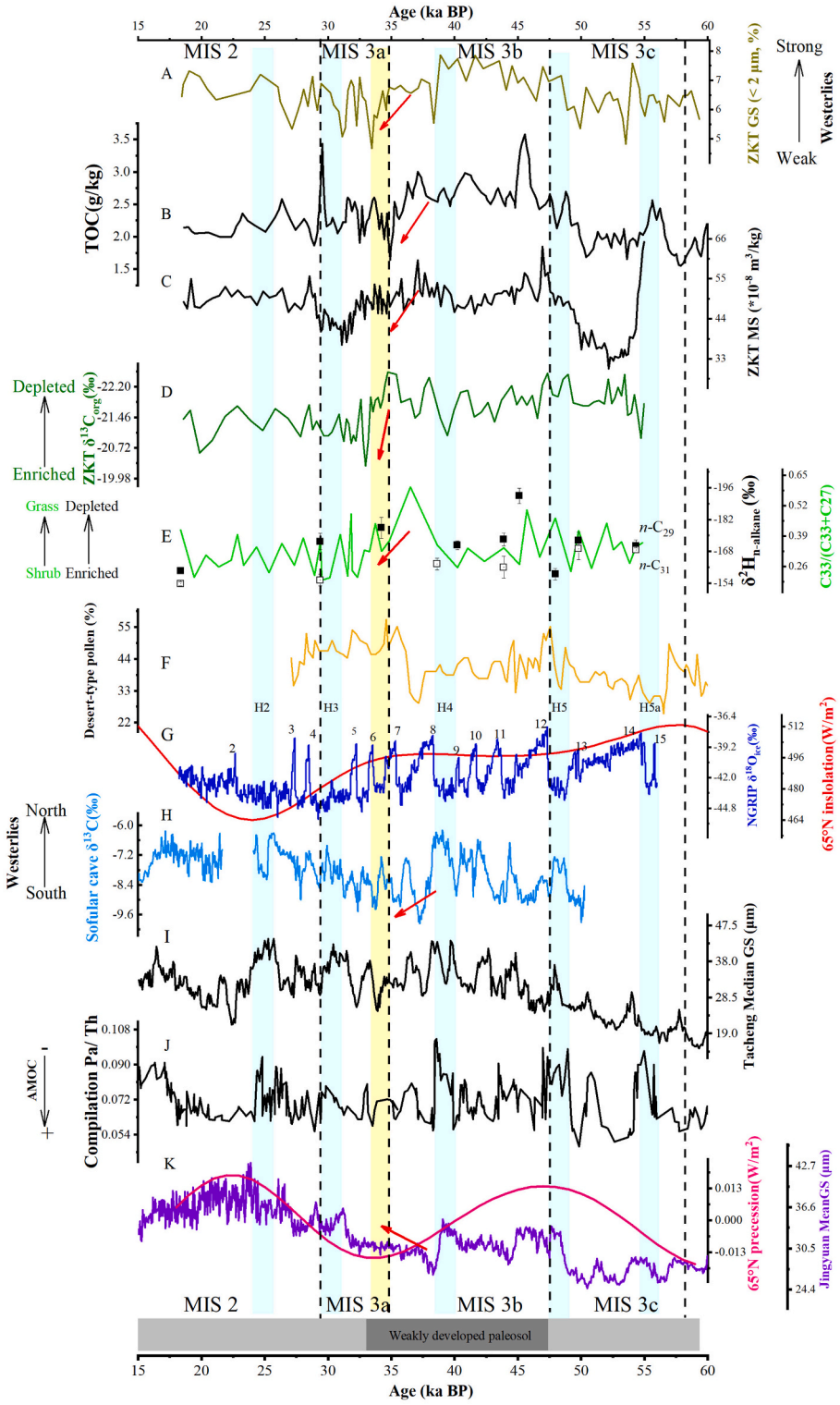

Fig. 3. Comparison of climate records during MIS3. (A) content of <2 μm grain size fraction in the Zeketai loess (E et al., 2014); (B) Total Organic Carbon content (TOC) of Zeketai loess (E et al., 2014); (C) magnetic susceptibility (this study); (D) $\delta^{13}C_{org}$ record of Zeketai Loess (this study); (E) *n*-alkane index of grass/shrub = $C_{33}/(C_{33}+C_{27})$ (this study) and hydrogen isotope composition of *n*-alkanes (δ^2H_{nC29} in filled square, δ^2H_{nC31} in open square; this study); (F) pollen percentage in sediment core BLK11A from Balikun Lake (Zhao et al., 2017); (G) Change of Northern Hemisphere summer insolation (21 June) at 65° N (Laskar et al., 2004), NGRIP ice core $\delta^{18}O$ (North Greenland Ice Core Project members, 2004), Arabic numbers: Interstadials warm events; H: Heinrich cold events.; (H) Westerlies swing indicated by Sofular cave $\delta^{13}C$ (Fleitmann et al., 2009); (I) median grain size of Tacheng loess (Li et al., 2019); (J) AMOC strength from Pa/Th of bulk sediment (Henry et al., 2016); (K) precession (Laskar et al., 2004) and the mean grain size (GS) of Jingyuan loess in the western CLP, indicating the intensity of SH (Sun et al., 2010).

powder with a ceramic mortar, and then passed through a 250 μm-mesh sieve to remove impurities such as plant roots. About 5 g of the ground and homogenized sample was analyzed using a Bartington MS2 magnetic susceptibility meter at low frequency (470 Hz), with the apparatus producing an alternating magnetic field of 200 A/m. To ascertain reproducibility, the samples were measured in triplicate. All reported values are based on the average of these measurements and corrected for the density of the samples.

2.3. Bulk stable organic carbon isotope analysis

Samples were selected at 10 cm intervals spanning from 2 m to 11.2 m for total organic carbon isotope analysis. Plant roots and large particles were removed from the samples, which were then mechanically crushed and fully ground to a uniform powder, subsequently sieved through a 75 μm-mesh sieve. About 2–3 g of each powdered and homogenized sample was treated with HCl to remove carbonates, following which 6–8 mg of each treated sample was wrapped into tin cups. The samples were analyzed with an MAT-253 isotope mass spectrometer (Thermo Fisher Scientific), using national standards (GBW04407 and GBW04408 black carbon). The measured carbon isotopic values of the samples are expressed in $\delta^{13}C$ relative to the V-PDB standard.

2.4. Lipid and compound-specific hydrogen isotope analysis

A total of 45 samples were chosen at a resolution of ca. 1 ka, including additional samples spanning the interval of 31–35 ka for lipid analysis. About 23–80 g of each sample was mixed with quartz sand and extracted with an accelerated solvent extraction instrument (Thermo Scientific Dionex ASE 100) using a mixture of dichloromethane and methanol (9:1, *v*/v). The obtained lipid extracts were evaporated to near dryness through a rotary evaporator, and then further dried under a gentle stream of nitrogen gas. The total lipid extract was separated over an activated silica gel column into a non-polar fraction (*n*-alkanes) by eluting with *n*-hexane, and a polar fraction by eluting with methanol. The non-polar fractions, containing the *n*-alkanes, were dissolved in *n*-hexane and analyzed using a Shimadzu Gas Chromatograph GC2010, equipped with a ZB-5MS quartz capillary column (60 m × 0.25 mm × 0.25 μm). The initial oven temperature was set at 70 °C, progressively raised to 210 °C at 10 °C/min, then raised to 300 °C at 3 °C/min, and maintained for 46 min. The inlet temperature was set at 300 °C, splitless, with helium as carrier gas. The temperature of the flame ionization detector (FID) was set at 320 °C.

The carbon preference index (CPI), capturing the predominance of odd-numbered compounds over even-numbered compounds, was calculated according to Marzi et al. (1993) based on the abundances of C_{25}-C_{33} *n*-alkanes.

The hydrogen isotopic compositions of *n*-alkanes in 14 samples were measured with a GC isotope ratio mass spectrometer (GC-IRMS; Thermo Trace Ultra GC coupled to a Delta V Advantage IRMS). The GC was equipped with a DB-5 MS column (30 m × 0.25 mm I.D. × 1 μm film thickness). Helium was used as the carrier gas at a constant flow of 1 mL/min. The heating program of GC oven was as follows: 50 °C (held for 1 min) to 210 °C at 10 °C/min (held for 2 min), then elevated to 300 °C at 4 °C/min (held for 2 min), and finally to 310 °C at 10 °C/min. The GC injector was set at 280 °C with splitless mode. The high-temperature conversion system (HTC-reactor tube f.H_2, Thermo Scientific) was carried out at 1400 °C. The δ^2H values were calculated against an internal standard (squalane, δ^2H -167‰). An in-house standard (containing C_{23}, C_{25}, C_{27}, C_{29}, C_{31}, and C_{33} *n*-alkanes) was analyzed between every four runs to examine instrument status. The H_3^+ factor was almost constant (standard deviation < ±0.1) during the sample runs. Standard deviations for $\delta^2H_{n\text{-alkanes}}$ were < 5‰ based on at least duplicate analysis of each sample. $\delta^2H_{n\text{-alkanes}}$ results are reported relative to Vienna Standard Mean Ocean Water (VSMOW).

3. Results

3.1. Magnetic susceptibility

The low-frequency susceptibility of the Zeketai profile ranged from 30.30×10^{-8} to 65.11×10^{-8} m^3/kg, with an average value of 46.99×10^{-8} m^3/kg. The magnetic susceptibility is generally higher in the paleosol layer compared to the loess layers (Fig. 3C). Specifically, magnetic susceptibility is lowest during MIS3c, and it subsequently rises in the paleosol layer representative of MIS3b, and maintains stability until ~35 ka, after which it begins to decrease. Subsequently, from around 30 ka onwards, there is another rise in magnetic susceptibility, persisting in a stable state from ~27 ka.

3.2. Bulk organic carbon stable isotope ratios

The $\delta^{13}C_{org}$ values across the Zeketai loess section display a range between −22.6 ‰ and − 20.3 ‰, averaging at −21.6 ‰ (Fig. 3D). The more negative $\delta^{13}C_{org}$ values are predominantly concentrated in the lower part of the record, dating back older than 35 ka. Around 35 ka, the $\delta^{13}C_{org}$ shifts discernibly to more positive values.

3.3. Plant leaf waxes in the Zeketai loess section

Higher plant-derived *n*-alkanes are present in all samples and are characterized by an odd-over-even distribution, of which *n*-C_{29} and *n*-C_{31} generally have the highest fractional abundance. The odd-over-even distribution is reflected by CPI values between 1.8 and 6.9, with an average of 4.3. The CPI remains relatively low until ~35 ka, beyond which there is a gradual increase into the late MIS3. The CPI values >1 indicate a higher plant source for *n*-alkanes and/or the relative immaturity of the organic matter.

The ratio of C_{27}/C_{31} predominantly remains <1.0 except for one sample (1.76 at 32.3 ka). The ratio of $(C_{27} + C_{29})/(C_{31} + C_{33})$ varies between 0.84 and 2.26 throughout the record, and undergoes a pronounced increase at the end of MIS3b around 37–32 ka when the ratio of C_{27}/C_{31} shows a similarly sharp rise. The ratio values of $C_{33}/(C_{33} + C_{27})$ (Fig. 3E) consistently stand higher than 0.2, with a slight increase and then a decreasing trend overall, notably decreasing during 37–32 ka.

Only nine samples have abundant nC_{29} and five samples have abundant nC_{31} for δ^2H analysis. The δ^2H_{nC29} ranges between −158‰ and −192‰ (Fig. 3E), indicating an overall deuterium-enriched trend during the late MIS3. Similarly, the δ^2H_{nC31} values range between −154‰ and −169‰, exhibiting a parallel deuterium-enriched trend during the late MIS3.

4. Discussion

4.1. Millennial-scale changes in (hydro)climate in northern Central Asia

Magnetic susceptibility can be influenced by the provenance of the loess, sedimentary processes, post-depositional weathering, and biological activity, but it is generally interpreted as a measure for pedogenesis, where magnetic susceptibility increases as a result of the development of fine-grained secondary magnetic minerals during soil formation (Zhou et al., 1990). Soil formation is thought to be enhanced during interstadials and interglacial periods due to the prevailing humid climate conditions at those times. On the CLP, magnetic susceptibility is used to trace glacial-interglacial variability in monsoon climate, where high magnetic susceptibility is linked to warm and wet climate conditions during times with a strong EASM (e.g., Ding et al., 2002; Vandenberghe et al., 2006). In the Ili basin, while the pedogenesis of loess deposits is generally moderate (Song et al., 2010), the weakly formed paleosol can be recognized in the χ_{lf} magnetic susceptibility record of the Zeketai section at 6–9 m (34. 8 ± 2.9 ka to interpolated ~47.8 ka) (Fig. 3C). This suggests a wetter climate condition occurred during this

time interval. Indeed, Wang et al. (2019) attributed the similar trends in clay content and χ_{lf} in a loess section of the Ili Basin to the formation of secondary ferrimagnetic minerals during pedogenesis, which can be in turn linked to precipitation. The loess of the Zeketai section during MIS3b was subjected to significant pedogenesis while χ_{lf} of the loess during MIS3a and MIS3c were probably affected dominantly by the provenance.

An alternative hypothesis is that, beyond hydroclimate influences, variations in magnetic susceptibility within a section could reflect shifts in sediment provenance featuring a distinct content of primary magnetic minerals (Jia et al., 2013). Furthermore, in arid areas with weak pedogenesis, such as CA, changes in magnetic susceptibility have been linked to wind velocity (Zeng et al., 2019). Following this scenario, higher magnetic susceptibility corresponds to the preferential mobilization of coarse magnetite during periods of strong winds, creating the opposite pattern to that commonly observed on the CLP (Beget and Hawkins, 1989; Song et al., 2010), which can be proved by a concordance between the χ_{lf} magnetic susceptibility (Fig. 3C) and the grain size records (Fig. 3A). However, there is an exception during MIS3b at the Zeketai profile. Similarly, the temporal pattern of TOC content (Fig. 3B) aligns well with that of χ_{lf} magnetic susceptibility within the Zeketai profile, except for the anomalous low values observed during MIS3b. The explanation is that magnetic susceptibility may be to an extent affected by local winds, albeit that it is primarily dependent on the Westerly. During stadials (i.e. MIS3a, MIS3c), westerlies transported coarser dust particles from source areas. The interstadial (MIS3b) experienced intensified local winds, facilitating the transportation of local material with fewer detrital magnetic minerals, and consequently yielding reduced magnetic susceptibility values (Zeng et al., 2019).

The Zeketai $\delta^2H_{n\text{-alkane}}$ record (Fig. 3E) exhibits an enriched trend during the late MIS3. The influence of vegetation type changes on $\delta^2H_{n\text{-alkane}}$ values will be addressed in 4.2. Regarding evapotranspiration, δ^2H values of leaf water and plant waxes are less relevant in the Ili Basin since *n*-alkanes are synthesized during leaf flush in spring (Kahmen et al., 2013) when it is still cold. Plant wax δ^2H values correlate well with the isotopic composition of precipitation (Sachse et al., 2012), suggesting that the Zeketai $\delta^2H_{n\text{-alkane}}$ record primarily reflects fluctuations in precipitation isotopes. This enriched trend aligns with the aridification pattern implied by magnetic susceptibility during the late MIS3.

High-latitude ice core records further substantiate that the climate shifted from interglacial D—O 7 to ice age level at 35 ka (Fig. 4A). Long-term transient simulations of mean annual precipitation in CA depict a decreasing trend until 35 ka (Fig. 4B, Li et al., 2013). The climatic oscillations around 35 ka are manifested in various northern CA regions, evidenced by comparisons of grain size and other proxies in multiple loess profiles. These profiles encompass the Nilek loess profile at Kashi River terrace in Ili (Fig. 4C, Li et al., 2018), the Tacheng Loess profile in Tacheng Basin (Fig. 4D, Li et al., 2019), the Zeketai loess profile of Xinyuan County in eastern Ili Basin (ZKT; Fig. 4E&F, E et al., 2014 and this study), the Taled Loess profile (TLD; Fig. 4G, Zhang et al., 2015), and the Zhaosu Poma profile in the upper reaches of the Tex River (ZSP; Fig. 4H&I, Song et al., 2018). Changes in mineral content and particle size components reveal the occurrence of abrupt climatic events, while increased quartz content suggests the occurrence of cold events in these loess profiles (Fig. 4H, Song et al., 2018). Likewise, the '35 ka' drought event in the ZKT loess profile could be identified by the decreased fraction of fine particles (Fig. 4E&G&I) or an increased fraction of coarse particles (Fig. 4C&D).

4.2. Vegetation response to hydroclimatic changes in Central Asia

A recent inventory on the impact of climate change on the vegetation cover and composition in C A showed that vegetation was most sensitive to precipitation, particularly in areas with shrubs or sparse vegetation (Jiang et al., 2017). In this context, we extrapolate the response of vegetation to hydroclimate fluctuations in the Ili basin during MIS3, based on changes in the stable carbon isotopic composition of the total organic carbon in the Zeketai loess section, as well as the distribution of plant leaf wax *n*-alkanes. Soil organic carbon, largely consisting of decomposed vegetation, offers a time-integrated representation of regional vegetation (Jobbagy and Jackson, 2000). Based on the photosynthetic pathway that causes a distinct fractionation of atmospheric CO_2, the relative contribution of C_3 and C_4 plants can be identified based on their $\delta^{13}C$ value (Farquhar et al., 1989). In Asia, C_3 plants are characterized by an average $\delta^{13}C$ value of -25.3 ± 0.3‰ and C_4 plants exhibit a value of -11.1 ± 1.5‰ (e. g., Passey et al., 2009). Following this principle, variations in $\delta^{13}C_{org}$ in loess-paleosol sequences from e.g., the CLP (An et al., 2005; Yang et al., 2015), CA(Rao et al., 2013; Shen et al., 2018) and southeastern Europe (Hatté et al., 2013; Wang et al., 2019), have been used to reconstruct past change in C_3 vs C_4 vegetation, where the contribution of C_4 vegetation generally increases during the warm and wet interglacials. The $\delta^{13}C_{org}$ values of the Zeketai loess section vary between -22.6 ‰ and -20.3 ‰ (Fig. 3D), indicating that C_3 plants were dominant. The shift in $\delta^{13}C_{org}$ towards more positive values around 35 ka suggests an increased contribution of C_4 plants (Fig. 3D). However, despite the tolerance of C_4 plants to arid conditions, their growth necessitates high seasonal temperatures, as they are outcompeted by C_3 plants at temperatures <15 °C (Huang et al., 2001). Indeed, Rao et al. (2013b) suggested that the mean annual temperature (MAT) of the Ili basin would have been inadequate for C_4 vegetation to thrive at this time (the MAT at Xinyuan city close to the ZKT profile is ~8 °C). Hence, the loess $\delta^{13}C_{org}$ signal mostly represents changes in vegetation composition in response to variations in precipitation, aligning with the findings of multiple investigations linking $\delta^{13}C_{org}$ values of C_3 plants and modern surface soils to the amount of precipitation (Diefendorf et al., 2010; Rao et al., 2017). In arid conditions, the diminished opening time of leaf stomata influences the CO_2 concentration ratio between the leaf and the atmosphere, consequently impacting the degree of fractionation (Diefendorf et al., 2010; Farquhar et al., 1989). In addition, a negligible contribution of C_4 vegetation in the Ili basin during MIS3 is also in agreement with the distribution of modern C_4 plants in China (Yin, 1997). Thus, the abrupt change in $\delta^{13}C_{org}$ of ~2.3 ‰ at ~35 ka is likely caused by a change in C_3 vegetation type resulting from the decrease in moisture availability at this time, as indicated by the magnetic susceptibility record (Fig. 3C).

To further elucidate the source of changes in $\delta^{13}C_{org}$ at Zeketai, we also analyzed *n*-alkanes, preserved in the same section. Leaf waxes, synthesized by higher plants as a protective mechanism against undesirable moisture loss, are generally well preserved in the geological record (e.g., Eglinton and Hamilton, 1967; Haggi et al., 2019; Zhang et al., 2006). Variations in *n*-alkane chain lengths are commonly utilized to deduce shifts in vegetation types on a local scale, assuming that plants synthesize longer-chain alkanes under warm and arid conditions, whereas *n*-alkanes with shorter chains are produced by more shrubs and fewer herbs (Bush and McInerney, 2013). Considering that both herbaceous and woody plants produce C_{29} and C_{31} *n*-alkanes (Bush and McInerney, 2013), a ratio including *n*-C_{27} and *n*-C_{33} alkanes would be a more accurate way to estimate the relative proportions of these two plant types. This approach is substantiated by Liu and Liu (2015), who combined >1200 observations of *n*-alkane data in grasses and woody-plants/shrubs from central China and found that herbaceous vegetation is represented by $C_{33}/(C_{33} + C_{27}) > 0.2$.

At Zeketai, *n*-alkane distributions vary in concert with $\delta^{13}C_{org}$, suggesting that the $\delta^{13}C_{org}$ primarily reflects vegetation change (Fig. 3D). Specifically, the ratios of *n*-alkanes $C_{27}/C_{31} < 1$ and $C_{33}/(C_{33} + C_{27}) > 0.2$ indicate the dominance of herbaceous plants, consistent with previous studies indicating the prevalence of desert-steppe and/or desert taxa vegetation during this period in Northwest China (Wei et al., 2015; Zhao et al., 2017). The ratios of $C_{33}/(C_{33} + C_{27})$ (Fig. 3E) decrease at 37–32 ka, suggesting a relative shift towards more shrubs. Notably, the modern δ^2H values in leaf waxes of shrubs are enriched, while those of

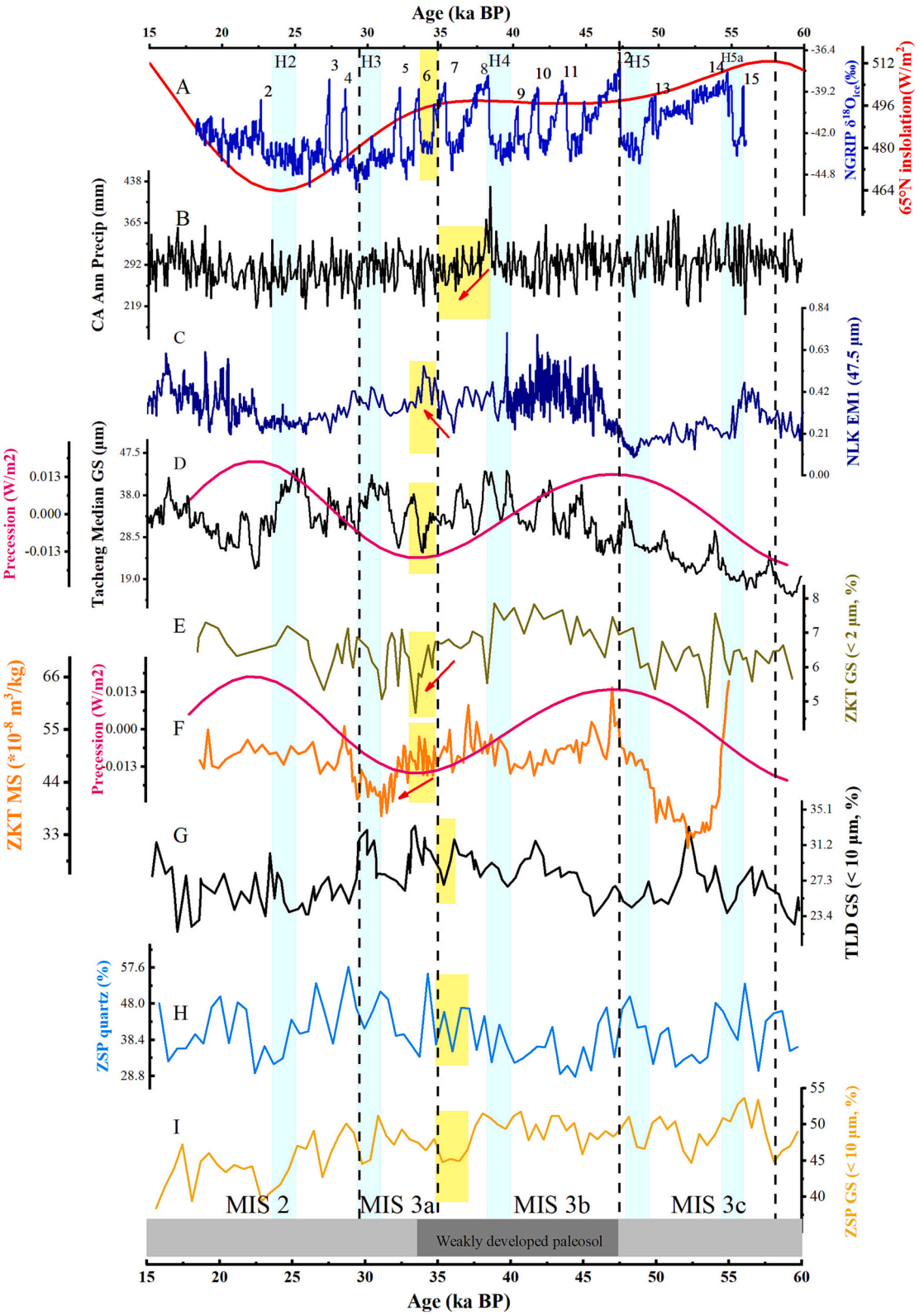

Fig. 4. Comparison of grain size(GS), magnetic susceptibility(MS), and mineral records of northern Central Asian loess with Greenland ice core oxygen isotope and other records during MIS3. Arabic numbers: Interstadial warm events; H: Heinrich cold events. (A) Northern Hemisphere summer insolation (21 June) at 65° N (Laskar et al., 2004), NGRIP ice core $\delta^{18}O$ (North Greenland Ice Core Project members, 2004); (B) modeled mean annual precipitation in CA (Li et al., 2013); (C) EM1 grain size variability in NLK loess (Li et al., 2018); (D) median grain size of Tacheng loess (Li et al., 2019); (E) grain size (< 2 μm) content in the Zeketai loess (E et al., 201414); (F) magnetic susceptibility in the Zeketai loess (this study); the precession (Laskar et al., 2004); (G) grain size (< 10 μm)content in TLD loess (Zhang et al., 2015); (H) quartz and (I) grain size (< 10 μm) content in ZSP loess (Song et al., 2018).

grasses tend to be more depleted (Liu and Huang, 2005). The Zeketai δ^2H_{nC29} and δ^2H_{nC31} values (Fig. 3E) showed a deuterium-enriched trend, implying the transition to more shrubs. This trend is further corroborated by pollen records of a nearby sediment core from Lake Balikun, which showed an increase in pollen representing desert-type vegetation during the same time interval (Fig. 3F) (Zhao et al., 2017). Together, the simultaneous shifts in plant wax distributions, $\delta^2H_{n\text{-alkane}}$ (Fig. 3E) and $\delta^{13}C_{org}$ (Fig. 3D) recorded in the Zeketai loess imply a vegetation transition towards relatively more drought-resistant shrubs in response to reduced precipitation around ~35 ka. The trend from herbaceous vegetation during interglacials (warm/wet) to more shrubs during glacials (cold/dry) also occurs on the western/drier part of the CLP (Fuchs et al., 2022). This pattern is especially pronounced in regions where precipitation, rather than temperature, constitutes the principal driver of vegetation transformations.

4.3. *Possible mechanisms driving increased aridity in northern Central Asia during late MIS3*

The Ili Basin is surrounded by mountains on three sides and located in an area where the moisture source has been dominantly controlled by the Westerlies since the Eocene (Caves et al., 2015), and still is today (Aizen et al., 2001; Huang et al., 2013). The grain size of loess has been extensively employed as an indicator of historical wind speed and atmospheric circulation dynamics (An et al., 1991; Sun et al., 2012). Particularly within the Ili basin, the finer component (< 2 μm) of loess is considered to be an indicator for the intensity of the Westerlies (Li et al., 2022), resting on the premise that the cold and arid climate impedes soil development and thus the production of fine components. Hence, stronger Westerlies lead to an increased contribution of the fine loess component to the local, coarse(r) loess. In the Zeketai loess profile, the contribution of fine-grained loess (< 2 μm) was initially high but then decreased substantially from ~35 ka onwards (Fig. 3A), suggesting a weakening of the Westerlies. At ca. 35 ka, the decreasing summer insolation in the Northern Hemisphere (Fig. 3G) caused the low temperature in North Atlantic (Cacho et al., 1999). This cooling trend in the North Atlantic impeded evaporation from the Atlantic Ocean, a critical moisture source for northern CA. The reduced moisture influx, along with the diminishing Westerlies, led to decreased precipitation and concomitant weakening of pedogenesis, which is reflected by the concurrent decline in magnetic susceptibility as observed in the Zeketai loess record (Fig. 3C).

The Westerlies form a pivotal link connecting the North Atlantic and the hydroclimate in ACA (e.g., Herzschuh, 2006; Li et al., 2018). Modern meteorological investigations affirm that Xinjiang (the study area) and the adjacent arid zones receive substantial moisture contributions from the west (North Atlantic) (Yatagai, 2003; Huang et al., 2013). On longer timescales, the influence of the North Atlantic is illustrated by the good correspondence between trends in loess grain size content (< 2 μm, Fig. 3A) and the Greenland ice core $\delta^{18}O$ record (Fig. 3G), where larger contributions of the fine loess component (< 2 μm) correspond to less negative $\delta^{18}O$ values in the ice core record. Interestingly, the aridification in ACA at ~35 ka coincides with a shift towards more negative values in the Sofular/Soreq stalagmite $\delta^{13}C$ record from northwestern Turkey (Fig. 3H, Fleitmann et al., 2009). More negative $\delta^{13}C$ values reflect amplified contributions of C_3 vegetation above the cave, an outcome promoted by a warmer and wetter climate. This implies that when ACA experienced aridification, the Black Sea region encountered wetter conditions, suggesting that the Westerlies shifted southward (Voskresenskaya and Maslova, 2011) halfway MIS3.

The transition to arid conditions in ACA around 35 ka, attributed to shifts in the intensity of Westerlies, is intricately tied to the strength of AMOC (Fig. 5), as suggested by a loess sequence from the nearby Tacheng basin (Li et al., 2019). The median grain size in the Tacheng loess section (Fig. 3I) demonstrates a substantial correlation with the strength of the AMOC (Fig. 3J). Sedimentary Pa/Th records from the North Atlantic (Fig. 3J) show that the AMOC strengthened after 35 ka (Henry et al., 2016). Strong AMOC leads to a small meridional temperature difference between mid-and high latitudes, thereby inducing weaker westerly winds. This scenario, coupled with a diminished supply of water vapor sources, engenders less moisture transport to CA. Alongside the AMOC and the Westerlies, the Siberian High-pressure system (Fig. 3K) also influences wind dynamics and loess deposition in the eastern Ili Basin (Li et al., 2018). High-latitude cooling greatly enhances the strength of the Siberian High (Gong et al., 2006), leading to a shorter intra-annual effective control time for the westerlies and increasing aridity.

5. Conclusions

Around 35 ka, discernible shifts towards drier climatic conditions are evident within northern CA. This alteration in hydroclimate dynamics correspondingly resulted in a shift in vegetation, favoring the proliferation of C_3 shrubs. The contribution of more drought-resistant C_4 vegetation is considered minor due to the likely suboptimal temperatures for C_4 vegetation growth within the basin. On millennial timescales, precipitation in the Ili Basin is influenced by insolation, Siberian High and North Atlantic climate dynamics, where an increased intensity of AMOC corresponds to weakened Westerlies, subsequently leading to reduced moisture transport to CA. The rapid response to hydrological changes in northern CA highlights the sensitivity of CA to (future) climate change.

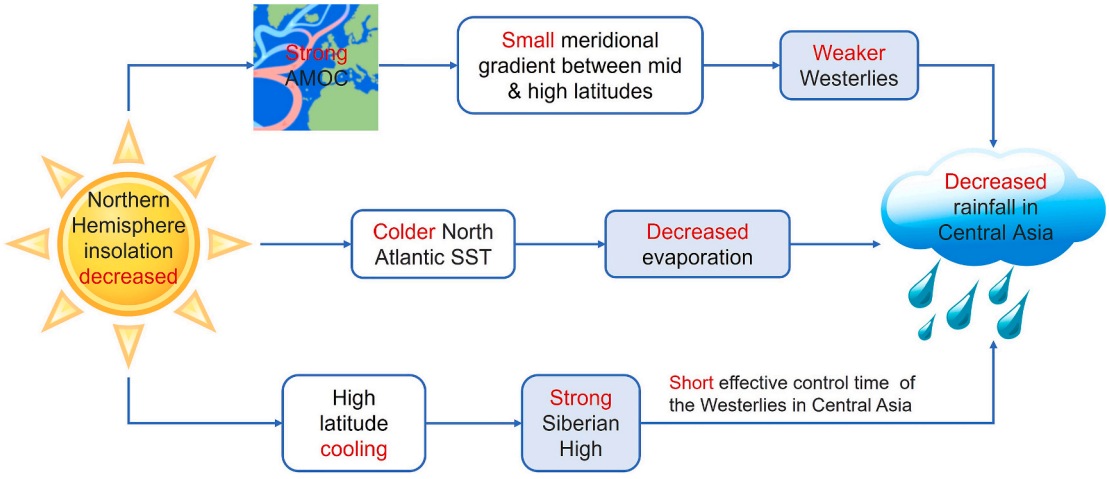

Fig. 5. Schematic diagram illustrating the physical mechanisms of moisture variations in northern Central Asia during late MIS3.

Declaration of Competing Interest

The authors declare that they have no known competing financial interests or personal relationships that could have appeared to influence the work reported in this paper.

Data availability

Data will be made available on request.

Acknowledgments

We would like to thank Dr. Zeng Fangming, who made this study possible. We also thank Prof. Huang Xianyu and Dr. Zhang Yiming, who helped with the GC-IRMS analysis. This work was supported by the National Natural Science Foundation of China (Grant No. 41830319 and 42073072).

References

Agosta, E.A., Compagnucci, R.H., 2016. Abrupt climate changes during the marine isotope stage 3 (MIS 3). In: Marine Isotope Stage 3 in Southern South America, 60 KA BP-30 KA BP, pp. 81–106.
Aizen, E.M., Aizen, V.B., Melack, J.M., Nakamura, T., Ohta, T., 2001. Precipitation and atmospheric circulation patterns at mid-latitudes of Asia. Int. J. Climatol. 21 (5), 535–556.
An, Z.H., Kukla, G.J., Porter, S.C., Xiao, J.L., 1991. Magnetic-susceptibility evidence of monsoon variation on the loess plateau of Central China during the last 130,000 years. Quat. Res. 36 (1), 29–36.
An, Z.S., Huang, Y.S., Liu, W.G., Guo, Z.T., Steven, C., Li, L., Warren, P., Ning, Y.F., Cai, Y.J., Zhou, W.J., 2005. Multiple expansions of C_4 plant biomass in East Asia since 7 Ma coupled with strengthened monsoon circulation. Geology 33 (9), 705–708.
Beget, J.E., Hawkins, D.B., 1989. Influence of orbital parameters on Pleistocene loess deposition in Central Alaska. Nature 337 (6203), 151–153.
Bush, R.T., McInerney, F.A., 2013. Leaf wax *n*-alkane distributions in and across modern plants: implications for paleoecology and chemotaxonomy. Geochim. Cosmochim. Acta 117, 161–179.
Cacho, I., Grimalt, J.O., Pelejero, C., Canals, M., Sierro, F.J., Flores, J.A., Shackleton, N., 1999. Dansgaard-Oeschger and Heinrich event imprints in Alboran Sea paleotemperatures. Paleoceanography 14 (6), 698–705.
Caves, J.K., Winnick, M.J., Graham, S.A., Sjostrom, D.J., Mulch, A., Chamberlain, C.P., 2015. Role of the westerlies in Central Asia climate over the Cenozoic. Earth Planet. Sci. Lett. 428, 33–43.
Chen, F.H., Yu, Z.C., Yang, M.L., Ito, E., Wang, S.M., Madsen, D.B., Huang, X.Z., Zhao, Y., Sato, T., Birks, H.J.B., Boomer, I., Chen, J.H., An, C.B., Wunnemann, B., 2008. Holocene moisture evolution in arid Central Asia and its out-of-phase relationship with Asian monsoon history. Quat. Sci. Rev. 27 (3–4), 351–364.
Chen, F.H., Xu, Q.H., Chen, J.H., Birks, H.J.B., Liu, J.B., Zhang, S.R., Jin, L.Y.Y., An, C.B., Telford, R.J., Cao, X.Y., Wang, Z.L., Zhang, X.J., Selvaraj, K., Lu, H.Y., Li, Y.C., Zheng, Z., Wang, H.P., Zhou, A.F., Dong, G.H., Zhang, J.W., Huang, X.Z., Bloemendal, J., Rao, Z.G., 2015. East Asian summer monsoon precipitation variability since the last deglaciation. Sci. Rep. 5, 1–11.
Chen, F., Chen, J., Huang, W., Chen, S., Huang, X., Jin, L., Jia, J., Zhang, X., An, C., Zhang, J., Zhao, Y., 2019. Westerlies Asia and monsoonal Asia: Spatiotemporal differences in climate change and possible mechanisms on decadal to sub-orbital timescales. Earth Sci. Rev. 192, 337–354.
Cheng, H., Edwards, R.L., Broecker, W.S., Denton, G.H., Kong, X.G., Wang, Y.J., Zhang, R., Wang, X.F., 2009. Ice age terminations. Science 326 (5950), 248–252.
Diefendorf, A.F., Mueller, K.E., Wing, S.L., Koch, P.L., Freeman, K.H., 2010. Global patterns in leaf ^{13}C discrimination and implications for studies of past and future climate. Proc. Natl. Acad. Sci. U. S. A. 107 (13), 5738–5743.
Ding, Z., Ranov, V., Yang, S., Finaev, A., Han, J., Wang, G., 2002. The loess record in southern Tajikistan and correlation with Chinese loess. Earth Planet. Sci. Lett. 200 (3–4), 387–400.
E, C.Y., Yang, T.B., Lai, Z.P., Sun, Y.T., Jiang, Y.Y., 2014. The environmental changes records since the last Glaciation at Zeketai loess section, Central Asia. J. Earth Environ. 5 (2), 163–172 (in Chinese with English abstract).
Eglinton, G., Hamilton, R.J., 1967. Leaf epicuticular waxes: the waxy outer surfaces of most plants display a wide diversity of fine structure and chemical constituents. Science 156 (3780), 1322–1335.
Farquhar, G.D., Ehleringer, J.R., Hubick, K.T., 1989. Carbon isotope discrimination and photosynthesis. Annu. Rev. Plant Physiol. Plant Mol. Biol. 40, 503–537.
Fleitmann, D., Cheng, H., Badertscher, S., Edwards, R.L., Mudelsee, M., Gokturk, O.M., Fankhauser, A., Pickering, R., Raible, C.C., Matter, A., Kramers, J., Tuysuz, O., 2009. Timing and climatic impact of Greenland interstadials recorded in stalagmites from northern Turkey. Geophys. Res. Lett. 36, L19707.
Fuchs, L., Zhou, B., Magill, C., Eglinton, T.I., Sun, Y., Peterse, F., 2022. Multiproxy records of temperature, precipitation and vegetation on the central Chinese Loess Plateau over the past 200,000 years. Quat. Sci. Rev. 288, 107579.
Gong, D.Y., Mao, R., Fan, Y.D., 2006. East Asian dust storm and weather disturbance: possible links to the Arctic Oscillation. Int. J. Climatol. 26 (10), 1379–1396.
Guo, Z.T., Ruddiman, W.F., Hao, Q.Z., Wu, H.B., Qiao, Y.S., Zhu, R.X., Peng, S.Z., Wei, J. J., Yuan, B.Y., Liu, T.S., 2002. Onset of Asian desertification by 22 Myr ago inferred from loess deposits in China. Nature 416 (6877), 159–163.
Haggi, C., Eglinton, T.I., Zech, W., Sosin, P., Zech, R., 2019. A 250 ka leaf-wax δD record from a loess section in Darai Kalon, Southern Tajikistan. Quat. Sci. Rev. 208, 118–128.
Hatté, C., Gauthier, C., Rousseau, D.D., Antoine, P., Fuchs, M., Lagroix, F., Marković, S. B., Moine, O., Sima, A., 2013. Excursions to C_4 vegetation recorded in the Upper Pleistocene loess of Surduk (Northern Serbia): an organic isotope geochemistry study. Clim. Past 9 (3), 1001–1014.
Henry, L.G., McManus, J.F., Curry, W.B., Roberts, N.L., Piotrowski, A.M., Keigwin, L.D., 2016. North Atlantic Ocean circulation and abrupt climate change during the last glaciation. Science 353 (6298), 470–474.
Hersbach, H., Bell, B., Berrisford, P., Horányi, A., Sabater, J.M., Nicolas, J., Radu, R., Schepers, D., Simmons, A., Soci, C., 2019. Global reanalysis: goodbye ERA-Interim, hello ERA5. ECMWF Newslett. 159, 17–24.
Herzschuh, U., 2006. Palaeo-moisture evolution in monsoonal Central Asia during the last 50,000 years. Quat. Sci. Rev. 25 (1–2), 163–178.
Huang, W., Chen, F.H., Feng, S., Chen, J.H., Zhang, X.J., 2013. Interannual precipitation variations in the mid-latitude Asia and their association with large-scale atmospheric circulation. Chin. Sci. Bull. 58 (32), 3962–3968.
Huang, Y., Street-Perrott, F.A., Metcalfe, S.E., Brenner, M., Moreland, M., Freeman, K.H., 2001. Climate change as the dominant control on glacial-interglacial variations in C3 and C4 plant abundance. Science 293 (5535), 1647–1651.
Jia, J., Xia, D., Wang, B., Zhao, S., Li, G., Wei, H., 2013. The investigation of magnetic susceptibility variation mechanism of Tien Mountains modern loess: Pedogenic or wind intensity model? Quat. Int. 296, 141–148.
Jiang, L., Bao, A., Guo, H., Ndayisaba, F., 2017. Vegetation dynamics and responses to climate change and human activities in Central Asia. Sci. Total Environ. 599, 967–980.
Jobbagy, E.G., Jackson, R.B., 2000. The vertical distribution of soil organic carbon and its relation to climate and vegetation. Ecol. Appl. 10 (2), 423–436.
Kahmen, A., Schefuß, E., Sachse, D., 2013. Leaf water deuterium enrichment shapes leaf wax *n*-alkane δD values of angiosperm plants I: Experimental evidence and mechanistic insights. Geochim. Cosmochim. Acta 111, 39–49.
Laskar, J., Robutel, P., Joutel, F., Gastineau, M., Correia, A.C.M., Levrard, B., 2004. A long-term numerical solution for the insolation quantities of the Earth. Astron. Astrophys. 428 (1), 261–285.
Li, Y., Song, Y.G., Lai, Z.P., Han, L., An, Z.S., 2016. Rapid and cyclic dust accumulation during MIS 2 in Central Asia inferred from loess OSL dating and grain-size analysis. Sci. Rep. 6, 6.
Li, X., Liu, X., Qiu, L., An, Z., Yin, Z.-Y., 2013. Transient simulation of orbital-scale precipitation variation in monsoonal East Asia and arid central Asia during the last 150 ka. J. Geophys. Res. Atmos. 118 (14), 7481–7488.
Li, Y., Song, Y.G., Fitzsimmons, K.E., Chang, H., Orozbaev, R., Li, X.X., 2018. Eolian dust dispersal patterns since the last glacial period in eastern Central Asia: insights from a loess-paleosol sequence in the Ili Basin. Clim. Past 14 (3), 271–286.
Li, Y., Song, Y.G., Yin, Q.Z., Han, L., Wang, Y.X., 2019. Orbital and millennial northern mid-latitude westerlies over the last glacial period. Clim. Dyn. 53 (5–6), 3315–3324.
Li, Y., Li, Y., Song, Y., Wei, H., Wang, Y., Shukurov, N., 2022. Effective moisture evolution since the last Glacial Maximum revealed by a loess record from the Westerlies-dominated Ili basin, NW China. Atmosphere 13 (11), 1931.
Liu, W., Huang, Y., 2005. Compound specific D/H ratios and molecular distributions of higher plant leaf waxes as novel paleoenvironmental indicators in the Chinese Loess Plateau. Org. Geochem. 36 (6), 851–860.
Liu, H., Liu, W., 2015. Relationship of plant leaf wax *n*-alkanes molecular distribution characteristics and vegetation types. J. Earth Environ. 6, 168–179 (in Chinese with English Abstract).
Marzi, R., Torkelson, B.E., Olson, R.K., 1993. A revised carbon preference index. Org. Geochem. 20 (8), 1303–1306.
North Greenland Ice Core Project members, 2004. High resolution record of Northern Hemisphere climate extending into the last interglacial period. Nature 431 (7005), 147–151.
Passey, B.H., Ayliffe, L.K., Kaakinen, A., Zhang, Z.Q., Eronen, J.T., Zhu, Y.M., Zhou, L.P., Cerling, T.E., Fortelius, M., 2009. Strengthened East Asian summer monsoons during a period of high-latitude warmth? Isotopic evidence from Mio-Pliocene fossil mammals and soil carbonates from northern China. Earth Planet. Sci. Lett. 277 (3), 443–452.
Rao, Z.G., Xu, Y.B., Xia, D.S., Xie, L.H., Chen, F.H., 2013. Variation and paleoclimatic significance of organic carbon isotopes of Ili loess in arid Central Asia. Org. Geochem. 63, 56–63.
Rao, Z.G., Guo, W.K., Cao, J.T., Shi, F.X., Jiang, H., Li, C.Z., 2017. Relationship between the stable carbon isotopic composition of modern plants and surface soils and climate: a global review. Earth Sci. Rev. 165, 110–119.
Sachse, D., Billault, I., Bowen, G.J., Chikaraishi, Y., Dawson, T.E., Feakins, S.J., Freeman, K.H., Magill, C.R., Mcinerney, F.A., Der Meer, M.T.J.V., 2012. Molecular paleohydrology: interpreting the hydrogen-isotopic composition of lipid biomarkers from photosynthesizing organisms. Annu. Rev. Earth Planet. Sci. 40 (1), 221–249.
Shen, X.Y., Wan, S.M., Colin, C., Tada, R., Shi, X.F., Pei, W.Q., Tan, Y., Jiang, X.J., Li, A. C., 2018. Increased seasonality and aridity drove the C_4 plant expansion in Central Asia since the Miocene-Pliocene boundary. Earth Planet. Sci. Lett. 502, 74–83.
Song, Y.G., Shi, Z.T., Fang, X.M., Nie, J.S., Naoto, I., Qiang, X.K., Wang, X.L., 2010. Loess magnetic properties in the Ili Basin and their correlation with the Chinese Loess Plateau. Sci. China-Earth Sci. 53 (3), 419–431.

Song, Y.G., Zeng, M.X., Chen, X.L., Li, Y., Chang, H., An, Z.S., Guo, X.H., 2018. Abrupt climatic events recorded by the Ili loess during the last glaciation in Central Asia: evidence from grain-size and minerals. J. Asian Earth Sci. 155, 58–67.
Sun, Y.B., Wang, X., Liu, Q., Clemens, S.C., 2010. Impacts of post-depositional processes on rapid monsoon signals recorded by the last glacial loess deposits of northern China. Earth Planet. Sci. Lett. 289 (1–2), 171–179.
Sun, Y.B., Clemens, S.C., Morrill, C., Lin, X.P., Wang, X.L., An, Z.S., 2012. Influence of Atlantic meridional overturning circulation on the East Asian winter monsoon. Nat. Geosci. 5 (1), 46–49.
Vandenberghe, J., Renssen, H., van Huissteden, K., Nugteren, G., Konert, M., Lu, H., Dodonov, A., Buylaert, J.-P., 2006. Penetration of Atlantic westerly winds into Central and East Asia. Quat. Sci. Rev. 25, 2380–2389.
Voskresenskaya, E.N., Maslova, V.N., 2011. Winter-spring cyclonic variability in the Mediterranean-Black Sea region associated with global processes in the ocean-atmosphere system. Adv. Sci. Res. 6 (1), 237–243.
Wang, Y.J., Cheng, H., Edwards, R.L., An, Z.S., Wu, J.Y., Shen, C.C., Dorale, J.A., 2001. A high-resolution absolute-dated late Pleistocene monsoon record from Hulu Cave, China. Science 294 (5550), 2345–2348.
Wang, Y.J., Cheng, H., Edwards, R.L., Kong, X.G., Shao, X.H., Chen, S.T., Wu, J.Y., Jiang, X.Y., Wang, X.F., An, Z.S., 2008. Millennial- and orbital-scale changes in the East Asian monsoon over the past 224,000 years. Nature. 451, 1090–1093.
Wang, P.X., Wang, B., Cheng, H., Fasullo, J., Guo, Z.T., Kiefer, T., Liu, Z.Y., 2017. The global monsoon across time scales: Mechanisms and outstanding issues. Earth Sci. Rev. 174, 84–121.
Wang, Q., Wang, X., Wei, H.T., Khormali, F., Xie, H.C., Zhang, J.H., Chen, F.H., 2019. Climatic significance of the stable carbon isotopic composition of surface soils in northern Iran and its application to an Early Pleistocene loess section. Org. Geochem. 127, 104–114.
Wei, H.C., Fan, Q.S., Zhao, Y., Ma, H.Z., Shan, F.S., An, F.Y., Yuan, Q., 2015. A 94-10 ka pollen record of vegetation change in Qaidam Basin, northeastern Tibetan Plateau. Palaeogeogr. Palaeoclimatol. Palaeoecol. 431, 43–52.
Xu, J.Z., Hou, S.G., Qin, D.H., Kaspari, S., Mayewski, P.A., Petit, J.R., Delmonte, B., Kang, S.C., Ren, J.W., Chappellaz, J., Hong, S.M., 2010. A 108.83-m ice-core record of atmospheric dust deposition at Mt. Qomolangma (Everest), Central Himalaya. Quat. Res. 73 (1), 33–38.
Yang, S.L., Ding, Z.L., Li, Y.Y., Wang, X., Jiang, W.Y., Huang, X.F., 2015. Warming-induced northwestward migration of the East Asian monsoon rain belt from the last Glacial Maximum to the mid-Holocene. Proc. Natl. Acad. Sci. U. S. A. 112 (43), 13178–13183.
Yatagai, A., 2003. Evaluation of hydrological balance and its variability in arid and semi-arid regions of Eurasia from ECMWF 15 year reanalysis. Hydrol. Process. 17 (14), 2871–2884.
Ye, W., Dong, G.R., Yuan, Y.J., Ma, Y.J., 2000. The climate instability of the last glacier in the Yili area, Xinjiang. Chin. Sci. Bull. 45 (6), 641–646 (in Chinese with English Abstract).
Yin, L.J., 1997. A study on the geographic distribution and ecology of C_4 plants in China: I. C_4 Plant distribution in China and their relation with regional climatic condition. Acta Ecol. Sin. 17, 350–363.
Zeng, M., Song, Y., Li, Y., Fu, C., Qiang, X., Chang, H., Zhu, L., Zhang, Z., Cheng, L., 2019. The relationship between environmental factors and magnetic susceptibility in the Ili loess, Tianshan Mountains, Central Asia. Geol. J. 54 (4), 1889–1901.
Zhang, Z., Zhao, M., Eglinton, G., Lu, H., Huang, C.-Y., 2006. Leaf wax lipids as paleovegetational and paleoenvironmental proxies for the Chinese Loess Plateau over the last 170 kyr. Quat. Sci. Rev. 25 (5–6), 575–594.
Zhang, W., Shi, Z., Liu, Y., Su, H., Niu, J., 2015. Climatic record in the loess-paleosol sediment in the Ili basin and comparative analysis with the Heinrich events. J. Glaciol. Geocryol. 37 (4), 973–979 (in Chinese with English abstract).
Zhao, Y.T., An, C.B., Duan, F.T., Zhao, J.J., Mao, L.M., Zhou, A.F., Cao, Z.H., Chen, F.H., 2017. Consistent vegetation and climate deterioration from early to late MIS3 revealed by multi-proxies (mainly pollen data) in Northwest China. Rev. Palaeobot. Palynol. 244, 43–53.
Zhao, J., An, C., Zhao, Y., Dong, W., 2022. Holocene C3/C4 vegetation variations in arid Central Asia: Implications for paleoclimate. Palaeogeogr. Palaeoclimatol. Palaeoecol. 592, 110905.
Zhou, L.P., Oldfield, F., Wintle, A.G., Robinson, S.G., Wang, J.T., 1990. Partly pedogenic origin of magnetic variations in Chinese loess. Nature 346 (6286), 737–739.